Cold-rolling effects on the microstructure properties of 316L stainless steel parts produced by Laser Powder Bed Fusion (LPBF)

L. Lemarquis, P. F. F Giroux, H. Maskrot, B. Barkia, O. Hercher, Philippe Castany

JOURNAL OF MATERIALS RESEARCH AND TECHNOLOGY 2021;15:4725–4736

Available online at www.sciencedirect.com

jmr&t Journal of Materials Research and Technology

journal homepage: www.elsevier.com/locate/jmrt

Original Article

Cold-rolling effects on the microstructure properties of 316L stainless steel parts produced by Laser Powder Bed Fusion (LPBF)

L. Lemarquis [a,*], *P.F. Giroux* [a], *H. Maskrot* [b], *B. Barkia* [b], *O. Hercher* [b], *P. Castany* [c]

[a] *Université Paris-Saclay, CEA, Service de Recherches Métallurgiques Appliquées, F-91191, Gif-sur-Yvette, France*
[b] *Université Paris-Saclay, CEA, Service d'Études Analytiques et de Réactivités des Surfaces, F-91191, Gif-sur-Yvette, France*
[c] *Univ Rennes, INSA Rennes, CNRS, ISCR – UMR 6226, F-35000, Rennes, France*

ARTICLE INFO

Article history:
Received 1 September 2021
Accepted 18 October 2021
Available online 23 October 2021

Keywords:
Additive manufacturing
Cold-rolling
LPBF
SLM
316L
Twinning

ABSTRACT

Laser Powder Bed Fusion (LPBF) technology provides new opportunities to enhance some piece-producing processes in the industry. Moreover, LPBF microstructures can heavily differ from microstructures usually obtained through traditional processes, especially 316L LPBF ones which combine both strength and ductility at room temperature. However, 316L LPBF microstructure evolution upon cold-rolling has not yet been extensively studied. In the present study, the effect of cold-rolling was investigated on the distinct 316L as-built microstructures showing different characteristics regarding mean grain size and texture. At first, LPBF 316L has sufficient ductility to be cold-rolled without any intermediate heat-treatments. Differences between initial microstructures affect the extent of grain refinement and texture decay. Indeed, the mean grain size and texture remain stable until 20% thickness reduction for one of the studied microstructure while they strongly decrease for the other one. Both microstructures show mechanical twinning after being cold-rolled with a twinned surface ratio exceeding 30%. Mechanical twins can also cross molten pool boundaries.

1. Introduction

Stainless steels are widely used in the industry. In this particular family, AISI 316L, along with the AISI 304L, are two of the most used austenitic stainless steel in chemical, petrochemical, pharmaceutical, shipping or food industries, especially for their good corrosion resistance in chloride environments and good wear resistance as well as their biocompatibility [1–3]. Their effective corrosion resistance comes from their chromium content at almost 18% in mass [4,5]. Moreover, 316L and 304L austenitic stainless steels are the main materials used in the nuclear industry for the structures related to the primary circuit of pressurised water

* Corresponding author.
E-mail address: louis.lemarquis@cea.fr (L. Lemarquis).
https://doi.org/10.1016/j.jmrt.2021.10.077

reactors [6]. One potential application of 316L steel is to compose complex-shaped tubes. According to Beck et al. [7], hexagonal-shaped tubes are considered to wrap the fuel pins in the proposed GenIV program. Currently, these tubes would be produced using standard processes, in which a classical cylindrical tube is drawn through a polygonal drawplate. One drawback is the heterogeneity in microstructure and mechanical properties between the angles and the flat surfaces of the polygon, in addition to the high production time [8,9]. This problematic issue is actually predominant in the production of non-cylindrical tubes in general with sharp angles.

Over the recent years, additive manufacturing (AM) techniques were improved drastically [10] and the Laser Powder Bed Fusion (LPBF) process is already used on industrial scale in the production of aerospace, automotive or aeronautical parts, such in the CFM LEAP engine [11–13]. The LPBF process appears as a strong alternative to conventional manufacturing processes, especially for complex-shaped parts in high value-added industries [11,14]. AM main assets remain in the following situation: (i) fast prototyping; (ii) reduction of material waste; (iii) simplification of the parts design; and (iv) simplification of the manufacturing process. LPBF 316L stainless steel was extensively studied and several characteristics differ from the conventional wrought 316L steel. At first, as-built parts show generally a strong anisotropy both for microstructural and mechanical properties due to an epitaxial growth upon building [15–19]. The degree of anisotropy can be influenced by both scanning strategies and process parameters [16]. Therefore, the tensile strength and the elongation decrease with the increase in the angle between the tensile loading direction and the laser scanning direction [17]. Ronneberg et al. [15] and Shifeng et al. [17] explained this anisotropy by the presence of molten pool boundaries (MPBs). Nevertheless, 316L LPBF parts show a good ductility while also having a stronger mechanical resistance compared to conventional 316L steel [20]. Two studies of the microstructure evolution after tensile deformations highlight that the high ductility is mainly promoted by mechanical twinning thanks to the low stacking fault energy [19,21]. This property is commonly observed in stainless steel alloys [22]. In addition to the mechanical twins role in the mechanical behaviour, the cellular sub-structure contributes to the 316L LPBF high strength compared to standard wrought 316L by retaining dislocations and interacting with deformation twins [21]. However, the aforementioned anisotropic properties, especially concerning large columnar grain presence and crystallographic texture, can be tailored and mitigated by modifying the process parameters. Sun et al. [23] reported a unique crystallographic lamellar microstructure for 316L LPBF while keeping a good relative density around 99.4%. They used a bidirectional scan without rotation from one layer to another. Formations of ⟨001⟩ and ⟨011⟩ crystallographic textures in LPBF 316L samples were also reported by changing laser powers from 380 to 950 W, affecting the tensile properties [24].

More recently, several studies have reported a different type of microstructure while using a Praxair-provided 316L powder [25–27]. This powder, while fulfilling all the 316L chemical norm requirements, is an argon-atomised powder, which is quite unusual as the majority of the powders are nitrogen-atomised. 316L steel made from this powder shows a much finer microstructure with less marked crystallographic texture, even considered as crystallographically isotropic according to Dryepondt et al. [26]. Interestingly, all the mentioned microstructures obtained from this powder are similar in texture, grain morphology and size, even if the machines and the selected process parameters are different. In addition, tensile tests showed a near isotropy regarding ultimate tensile strength, yield strength and uniform elongation, which is in good correlation with the microstructural properties [25,26]. The combination of high ductility and strength also come from the interaction between mechanical twins and the cellular sub-structure [26].

However, the LPBF building parameters should be carefully optimised in order to achieve the required mechanical performances and microstructure properties [24,28]. Indeed, some defaults such as residual porosity can affect the yield strength and the elongation to failure [15,19,29,30].

Concerning the aforementioned tubes, hexagonal-shaped preforms could be additively built with LPBF process and then cold worked (rolled, pilger milled or hammered) in order to obtain the final-shaped tubes. Therefore, the conventional manufacturing process would be optimised and simplified by reducing the number of working steps. Additionally, the final parts would have some of the LPBF 316L steel properties such as good ductility and high strength, and the porosity of LPBF parts would be reduced by cold deformations. Until now, cold-rolling as post-processing step was not explored, but a new hybrid forming technique combining LPBF and hot forging was recently investigated for 316L and Inconel 718 steels [31,32]. Hot forging allows reducing the porosity of additively manufactured preforms, as well as refining the microstructure. Moreover, effective grain recrystallization and pressure bonding the voids are believed to be at the origin of significant elongation and ultimate tensile strength (UTS) increases. Combination of hot forging (hot compression) on LPBF preforms was also investigated on Ti–6Al–4V [33–35]. The hot worked material shows a lower porosities density but also different microstructures depending on the parameters used during the heat treatment and the following hot compression. The final exhibited properties are similar to the conventional forging process chains. Therefore, new process chains, which allow reducing the forging steps, can be developed on TI–6AL–4V parts [35]. Furthermore, Bambach et al. [36] led investigations on the hot compression of Laser Metal Deposition (LMD) preforms of Inconel 718. LMD-produced IN718 appeared to be hot workable after heat treatment, showing similar yield and ultimate strength levels than the traditional wrought material. Other studies were based on the combination of Wire + Arc Additive Manufacturing (WAAM) and rolling of Ti–6Al–4V [37–39].

Nevertheless, no investigations were handled about LPBF parts cold workability, even though tensile deformation mechanisms were studied [19,21]. This study focuses on preliminary results about cold-rolled LPBF 316L steel. Two different microstructures were built by using two different powders and sets of parameters: one exhibiting large columnar grains and the other more equiaxed ones [25]. The as-built preforms were cold-rolled at different strains along the building direction. These both microstructures are original compared to standard wrought 316L and applying a cold

deformation can lead to original properties, which cannot be achieved with standard 316L. The different obtained microstructures were observed and studied by SEM-EBSD and optical microscopy. The main goal of this paper is then to study the evolution of these two different microstructures, including crystallographic texture, upon cold rolling as well as the activated deformation mechanisms.

2. Materials & methods

2.1. Preforms building

The 316L stainless steel rectangular shaped preforms ($60 \times 20 \times 15$ mm^3) were manufactured from two different powders and on two different LPBF machines. One powder is provided by SLM Solutions which was used on a Trumpf TruPrint Series 1000 printer; the other one provided by Praxair was used on an SLM Solutions GmbH 280^{HL} 3D printer. All the samples were processed under Argon atmosphere. The process parameters used on the TruPrint 1000 machine were optimised in a previous study [25] to achieve a relative density of more than 99.5% (measured with the Archimede's method) and get two drastically different microstructures, which will be presented in the Results section. The optimised AM process parameters [25] are given in Table 1.

As mentioned in Table 1, the scan strategy used in the SLM280^{HL} machine was developed by SLM Solutions. It consists of a raster scanning strategy with 7 mm-wide strips and a rotation angle of 67° between two consecutive layers. Additional limitations about the orientation of the strips in relation to the argon flux were implemented, limiting the slag deposition during construction. A relative density of 99.7% was achieved using this set of parameters.

Table 2 presents the chemical compositions measured on both powders [25]. Oxygen and nitrogen contents were measured specifically for this study by a Horiba EMGA-820AC chemical analyser.

The two considered powders show several discrepancies in terms of chemical composition. Indeed, the nitrogen, manganese, phosphorous and copper contents differ by around an order of magnitude between both powders. The difference in nitrogen content, almost changing the order of magnitude from 130 ppm in the Praxair powder to 1226 ppm in the SLM one, can be explained by the atomisation gas used as mentioned in the introduction (nitrogen atmosphere for SLM and argon atmosphere for Praxair). This difference is almost of the same amplitude in the as-built samples with 97 ppm and 847 ppm respectively (mean values of 7 measurements each). Chniouel [25] made a benchmark of 11 powders and only preforms built with the Praxair one exhibited a quasi-equiaxed microstructure.

Both powders were systematically sieved in a 50 μm-sieve and heated at 60 °C to remove humidity before use in the AM printer. Particle size measured by a Horiba Partica LA-950 analyser using the Fraunhofer laser diffraction method vary from $D_{10} = 22$ μm to $D_{90} = 45$ μm for both powders with similar D_{50} value equal to 31 μm.

In this study, only vertical preforms were built along the build direction, as shown in Fig. 1a. The as-built preforms were buffed and sanded to remove the building supports and for the surface finish.

In this paper, the samples and related microstructures obtained by consolidation of the SLM powder on the TruPrint 1000 machine will be named (A) and the one obtained from the Praxair powder on the SLM280^{HL} machine will be named (B). This paper is focused on the evolution of such microstructures, which can be obtained only through the LPBF process, during cold-rolling.

2.2. Cold rolling process

The as-built samples were subjected to cold rolling using a unidirectional rolling mill, which rollers turn at 34 rounds per minute. The rolling direction is collinear to the preforms building direction (Fig. 1b). Two rates of cold rolling reduction (10% and 20%) were investigated. At first, the sample was cold-rolled progressively step by step with reduction to 10%. A part of the preform was cut for the microstructure characterisation and the remaining part was rolled further with reduction to 20%. Additionally, both as-built samples (A) and (B) were cold-rolled to a maximum thickness reduction of 80% without any visible crack formation. Due to this high deformation level, it was not possible to obtain reliable observations of the

Table 1 – AM process parameters used for sample fabrication.

Machine	Power (W)	Spot diameter (μm)	Scan speed (mm/s)	Hatch spacing (μm)	Layer thickness (μm)	Scan strategy
Trumpf TruPrint 1000 (A)	150	55	675	90	20	Bidirectional with 90° rotation between two successive layers
SLM Solutions SLM280^{HL} (B)	175	75	750	100	30	Custom made by SLM Solutions

Table 2 – Chemical compositions of the two used 316L powders.

	Mass percentage (3% of incertitude)					Mass ppm				
Element	Cr	Ni	Mn	Mo	Si	O	N	P	S	Cu
SLM (A)	17.35	11.45	1.06	2.07	0.51	444	1226	300	130	2150
Praxair (B)	17.26	12.42	0.51	2.5	0.43	520	130	44	95	100

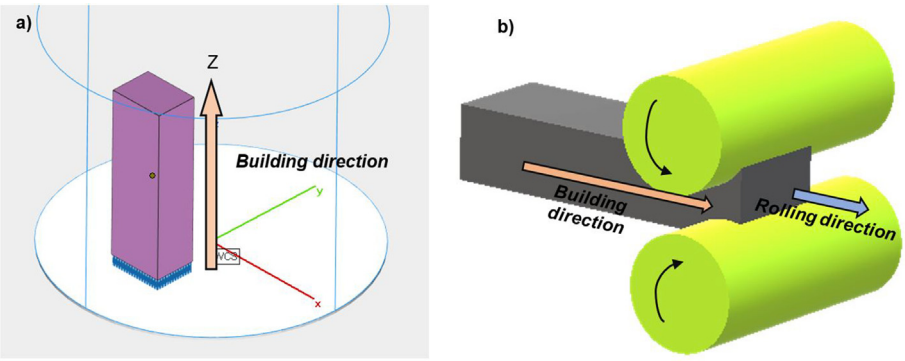

Fig. 1 – Schematic diagrams to illustrate the axes definition a) and the samples rolling pattern b).

microstructure by scanning electron microscopy (SEM) and electron backscattered diffraction (EBSD). The 80% cold-rolled specimen was then only performed to demonstrate the good cold-workability of as-built samples and no result will be presented for this metallurgical state.

2.3. *Microstructure characterisation*

The samples were mechanically grounded by SiC grinding papers until 4000 grit and then polished for 1 min with colloidal 3 μm-diamond solution to achieve a mirror surface finish. Then, an electrolytic polishing was performed for 35 s using a 10 wt% oxalic acid solution at 15 V on a Struers LectroPol-5 machine. An etching was also performed using a 10 wt% oxalic acid solution at 10 V for a duration ranging between 40 and 85 s depending on the microstructure and the applied rolling strains.

A Zeiss AXIO Image M2m optical microscope (OM) was used at first to check the microstructure. The OM images were taken by a Zeiss AXIO Cam ICc5. Grain orientation maps, local misorientation maps and pole figures were characterised by a SEM incorporating an Electron BackScattered Diffraction detector. Two different SEM were used: JEOL-7000F (FEG) and TESCAN VEGA-3 (W) with both Bruker detectors. EBSD analyses were performed using the same parameters: ≈15 kV acceleration voltage, approximately 10 μA current density depending on the microstructure and a step size ranging from 0.3 to 1.0 μm. The OM and IPFs images are taken in the (XZ) plane defined in Fig. 1a, along the building direction. To clean the maps and ensure a correct measurement of the grain size distributions, the wild spikes are removed and a grain inside misorientation cannot exceed 10°. A problem appears when the molten pool boundaries are not indexed due to the oxalic acid etching, so they cut a traversing grain into different grains. Thus, the grain size calculation would be skewed. Therefore, a rather important extrapolation was used to fill the gaps for the grain size calculation. Additionally, Σ3 boundaries are set as grain boundaries considering that practically all the detected Σ3 boundaries are grain boundaries on the SEM images at low magnification. For the Kernel Average Misorientation (KAM) calculations, only the wild spikes were removed while no extrapolation was done and the KAM grid is fixed at 5 × 5 pixels.

3. Results

3.1. *Microstructure morphology*

Fig. 2 presents an overview of the obtained microstructures at different magnifications. The oxalic acid etching reveals the grain boundaries and the cellular sub-structures. Thus, observations can be made on the microstructure morphology, before more detailed analyses in the subsequent sections.

Fig. 2a and b show the as-built microstructure of the sample (A) and the sample (B) respectively observed using OM. In microstructure (A), the grain length can exceed 200 μm and cross multiple molten pool boundaries (MPBs). The resulting microstructure is composed by columnar grains which are common for LPBF 316L stainless steel [15,40,41]. In the other hand, the microstructure (B) exhibits smaller grains with a diameter not exceeding 50 μm. These grains can also cross MPBs as in as-built microstructure (A). However, due to their size, grains of sample (B) do not cross multiple MPBs, just one in some cases. These features concerning MPBs are also visible when the material is cold-rolled at 20% strain as exposed in Fig. 2c and d.

An observation of the above microstructures at higher magnification using SEM shows the typical LPBF cellular sub-structure in the as-built state (Fig. 2e and f). This sub-structure remains when cold-rolled at higher strains.

Fig. 2c and d is OM observations of microstructures (A) and (B) cold-rolled at 20% strain. Their colours are turned into grey shades in order to highlight the microstructure features. The etching allowed to spot several twins in some grains, circled in orange on the figures, on both microstructures. Twins also cross through MPBs, as grains do.

Thus, both microstructures, despite their visible as-built differences, show mechanical twins visible in OM. Nevertheless, EBSD analyses are required to confirm these preliminary observations, especially about the grain size distribution and mechanical twinning.

3.2. *EBSD analysis: grain size and morphology*

Inverse pole figure maps along Y_{EBSD} (IPF) of multiple samples are presented in Fig. 3, with the as-built microstructures and

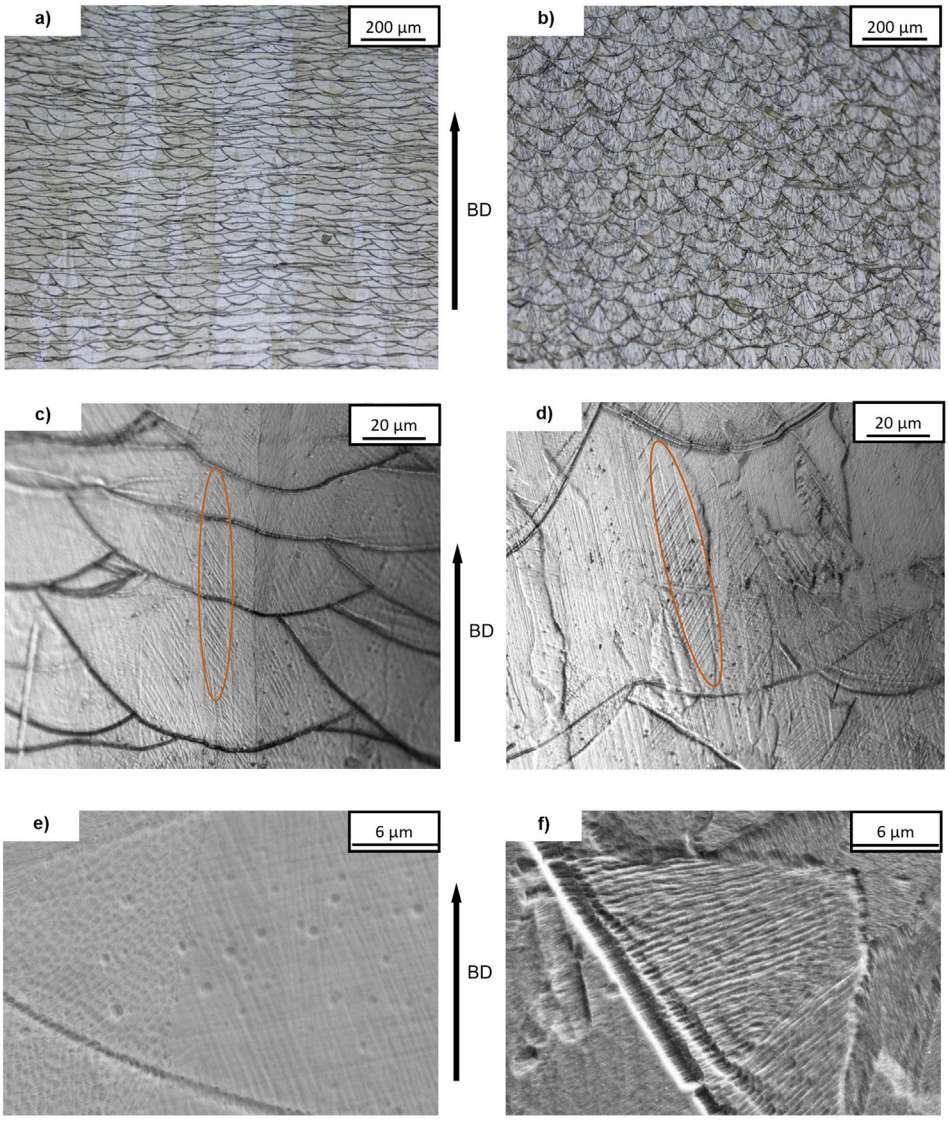

Fig. 2 – OM and SEM micrographs of microstructures (A) and (B): OM images of as-built samples (A) and (B), respectively a) and b), OM images of 20% cold-rolled samples (A) and (B), respectively c) and d), SEM images of as-built samples e) and (B) f). Orange-circled zones show the visible twins.

the 20% cold-rolled ones for both powders. For all EBSD-analysed samples, the Y_{EBSD} direction is collinear to the building direction, i.e. the Z-axis in Fig. 1a.

At first, no martensite is detected by EBSD on all the observed microstructures, even at higher magnification. All the presented microstructures are fully austenitic, even for 20% cold-rolled samples, which is consistent with previous observations for wrought 316L where strain-induced martensite appears starting from 30% to 40% of thickness reduction [42,43].

Fig. 3a confirms the observations made by OM for the sample (A) as the exhibited grains are columnar along the building direction. Some observed grains have a length higher than 300 μm. This type of grains is also visible on 10% and 20% cold-rolled microstructures (A), as shown in Fig. 3b. However, multiple small size grains appear during cold rolling, leading to a reduction of the grains mean diameter upon cold rolling. Indeed, the grains mean diameter decreases from 102 μm in the as-built state to 56 μm when cold-rolled at 20% as mentioned in Table 3. Nevertheless, elongated grains with grain length higher than 300 μm are still visible on the 20% cold-rolled sample (A). The predominance of columnar grains along the building direction Y_{EBSD} in the as-built sample (A) is also confirmed in Table 3 by the values of the mean main axis inclination θ compared to X_{EBSD}. θ ranging between 65.7° and 82.1° shows that the grains main axis are oriented towards the building direction. The microstructure is morphologically anisotropic, the mean aspect ratio evolving between 0.21 and 0.38. Therefore, the as-built microstructure (A) shows columnar grains along the building direction with an important aspect ratio as already observed [15,16,44]. Cold-rolling leads to a grain refinement but no trend can be drawn concerning the mean aspect ratio.

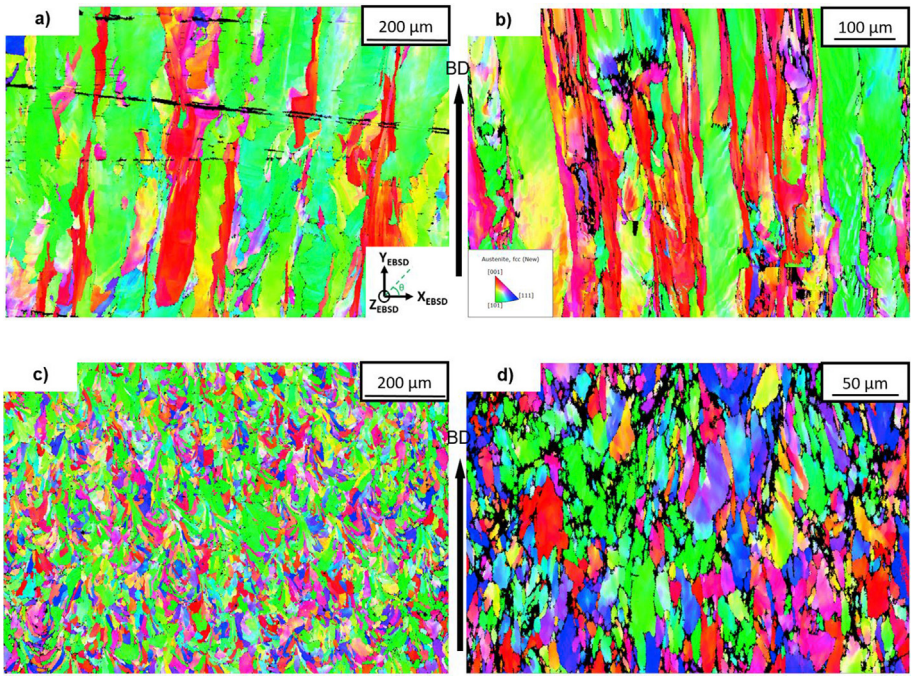

Fig. 3 – EBSD probed Inverse Pole Figure (IPF-Y) maps of the microstructure (A) in the as-built, a), and 20% cold-rolled, b), states and of the microstructure (B) in the as-built, c), and 20% cold-rolled, d), states. Step size: 0.3–0.9 µm. Building direction (Z-axis) = Y_{EBSD}.

Fig 3c shows the IPF-Y map of the as-built microstructure (B). The microstructure is composed of small and quasi-equiaxed grains at first glance, as previously reported [21,26]. The 20% cold-rolled microstructure (B) shown in Fig. 3d exhibits the same grain properties. According to the measurements shown in Table 3, the mean grain diameter does not change when the sample is cold-rolled, ranging between 20.3 and 21.8 µm. Furthermore, the grain aspect ratio tends to decrease from 0.43 in the as-built state to 0.34 after cold-rolled at 20%. In addition, the mean main axis inclination shows that the grains are rather oriented towards the building direction. Therefore, the increase in aspect ratio can be explained by the fact that the rolling direction is collinear to the building direction, hence the grain long axis.

Table 3 – Mean grain size weighted by area fraction and grain morphology depending on the microstructure type and the cold-rolled deformation rate. Grains at the IPF edges are removed from the calculation.

Sample	Grains mean diameter (µm)	Mean aspect ratio (width/length)	Mean grain main axis inclination θ	Number of analysed grains
As-built (A)	102 ± 2	0.29 ± 0.01	77.4° ± 0.1°	559
10% (A)	96 ± 1.7	0.38 ± 0.04	65.7° ± 0.8°	1377
20% (A)	56 ± 0.9	0.21 ± 0.01	82.1° ± 0.1°	597
As-built (B)	20.3 ± 0.1	0.43 ± 0.01	63.5° ± 0.1°	7721
10% (B)	21.8 ± 0.1	0.40 ± 0.01	72.0° ± 0.1°	6400
20% (B)	20.5 ± 0.3	0.34 ± 0.01	78.6° ± 0.1°	1070

These results show a different microstructure evolution when cold-rolled, especially concerning the grain mean diameter with a stark reduction by half between the as-built and the 20% cold-rolled states for sample (A), and no variation for sample (B).

3.3. *EBSD analysis: texture*

At first, some grains show no noticeable changes in their crystallographic orientation when crossing molten pool boundaries, both in the as-built (A) and the as-built (B) microstructures as shown in Fig. 3.

The as-built part (A) shows a heavily textured microstructure with ⟨110⟩ along the building direction (Fig. 4a). The same texture is observed when the preform is cold-rolled at 10% (Fig. 4b). However, the texture peak intensity is significantly lower after 10% thickness reduction than in the as-built state, from 20 to 8.4 while keeping the same calculation parameters. In addition, the maximum of the ODF figures decreases from 0.48 to 0.2. Therefore, the initial strong texture of sample (A) tends to be weakened by cold rolling.

The as-built microstructure (B) presents a texture with ⟨110⟩ along the building direction (Fig. 4c). But this texture intensity is weak and can be called as residual thanks to the low intensity on the pole figure (4.0) and the low ODF figure maximum value (0.12). Dryepondt et al. [26] considered the as-built microstructure (B) as effectively crystallographically isotropic. Cold-rolled samples (B) do not exhibit any preferential texture with the ODF figure maximum value ranging from 0.10 to 0.07. Therefore, the microstructure (B) keeps its crystallographic isotropy upon cold-rolling.

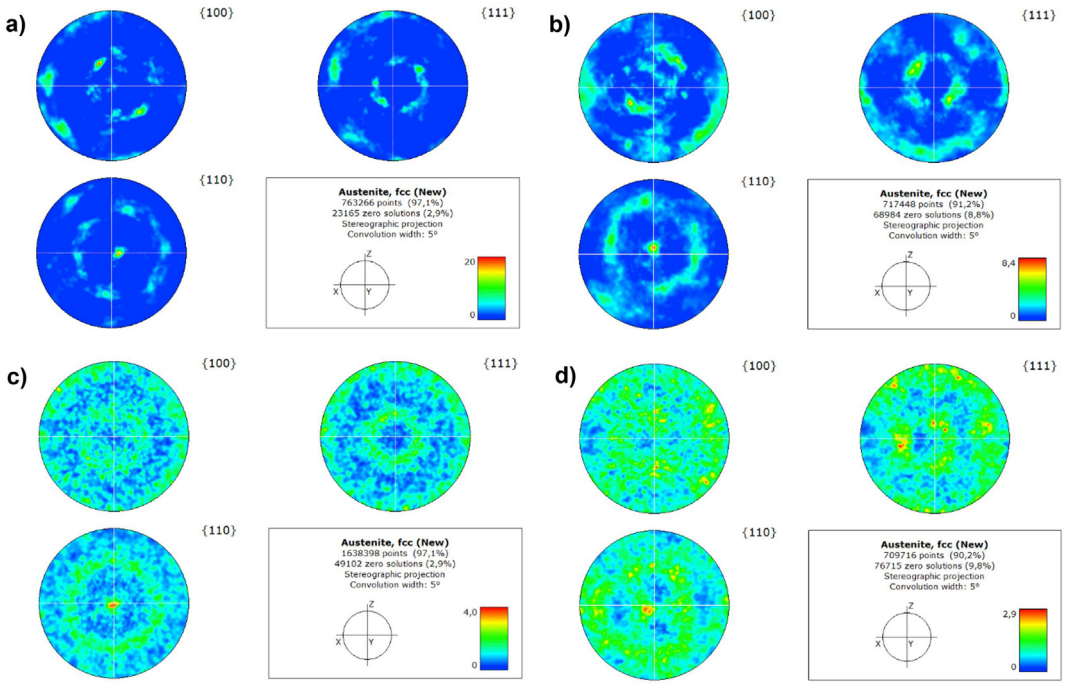

Fig. 4 – Corresponding pole figures from the IPF maps exposed in Fig. 3. As-built (A) a), 10% cold-rolled (A) b), As-built (B) c) and 20% cold-rolled (B) d). Building direction: Y_{EBSD}.

3.4. *EBSD analysis: local misorientation and twinning*

From the EBSD data, the KAM was computed in order to determine the local misorientation in the microstructure before and after cold-rolling.

Fig. 5a and b show the evolution of the KAM map of the sample (B) from the as-built state to 10% deformation. At first, the as-built microstructure shows already some residual local misorientation, which is in agreement with Wang et al. [40]. The comparison shows that the local misorientation increases with the rolling deformation. This increase between as-built and 10% cold-rolled states is shown in Fig. 5c as the local misorientation distribution peak shifts towards higher misorientation angles from 1.02° to 1.26° for sample (B). The full-width half-maximum (FVHM) increases from 0.76° in the as-built state to 1.31° in the 10% cold-rolled one. Therefore, the overall KAM distribution is shifted towards higher angles after cold rolling. This trend is confirmed at 20% cold-rolling as the KAM distribution is shifted even further with the peak at 1.85°.

The same trend was observed in sample (A). The as-built microstructure also shows some residual local misorientation. The KAM distribution is also shifted towards higher misorientation angles between the as-built and the 10% cold-rolled states: the distribution peak shifts from 1.33° to 2.08° and the FVHM increases from 1.22° to 2.74°. However, in both as-built and cold-rolled states, the local misorientation and the cold-rolling influence are higher in sample (A) than in sample (B), certainly due to the larger grains.

Additionally, EBSD analyses have also been performed on smaller areas of both samples with approximately $400 \times 300\ \mu m^2$. Fig. 6a presents the overlap between the band contrast and the IPFZ maps of the 10% cold-rolled sample (A). At first, thermal twins, with less than 10 μm width, are visible. These twins can be a result of the AM process as they are also present in as-built microstructures. Furthermore, some grains show many mechanical twins, confirmed by the 60° misorientation angle between the twins and the matrix. Interestingly, in this sample, mechanical twinning is activated in all the ⟨001⟩ oriented grains in red while only few grains oriented in other directions show evidence of mechanical twins. On this EBSD analysis, the surface fraction of mechanical twinned grains represents 40% ± 2% of the total surface.

The same EBSD analyses were conducted on samples (B), in order to observe potential mechanical twinning after cold rolling deformation. The as-built microstructure shows some thermal twins, as well as the cold-rolled ones. At 10% strain (Fig. 6b), several grains show mechanical twins. This trend is confirmed at 20% strain (Fig. 6c) where higher fraction of twins is observed. In fact, the twinned surface ratio increases from 31% ± 2% to 38% ± 2% between 10% and 20% deformation due to newly twinned grains. In addition, twins are wider in some grains, and wide enough to be detected in the IPF map. Therefore, at 20% strain, new grains are twinned and the already existing twins are supposed to get wider under further cold rolling deformation. Furthermore, some grains exhibit two mechanical twin variants at 20% strain (circled in orange in Fig. 6c), which is a consequence of further cold-rolling.

However, in both microstructures, these results confirm that twins and grains can cross molten pool boundaries without deviation.

To summarise, both microstructures (A) and (B) show mechanical twins when cold-rolled, as shown in optical microscopy images (Fig. 2), starting at 10% deformation but twinning could start at lower strain levels.

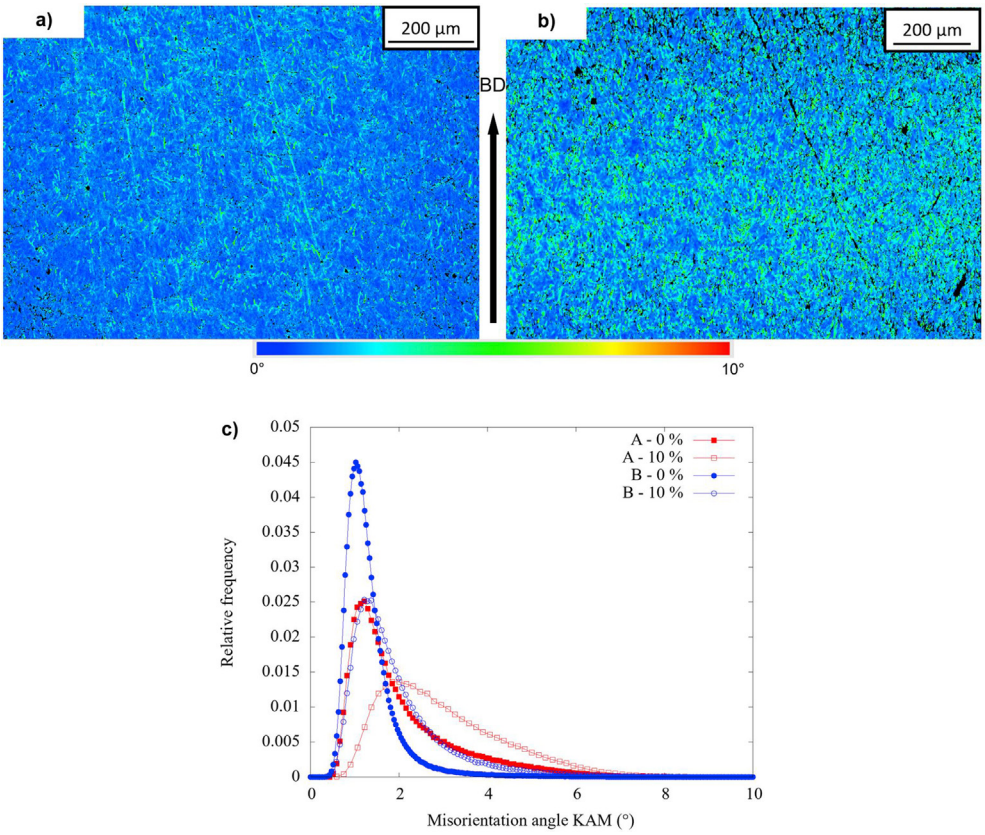

Fig. 5 – Kernel Average Misorientation (KAM) maps, measured in degrees, of the microstructure (B) in the as-built and 10% cold-rolled states, respectively a) and b). The different local misorientation angle distributions are shown in c).

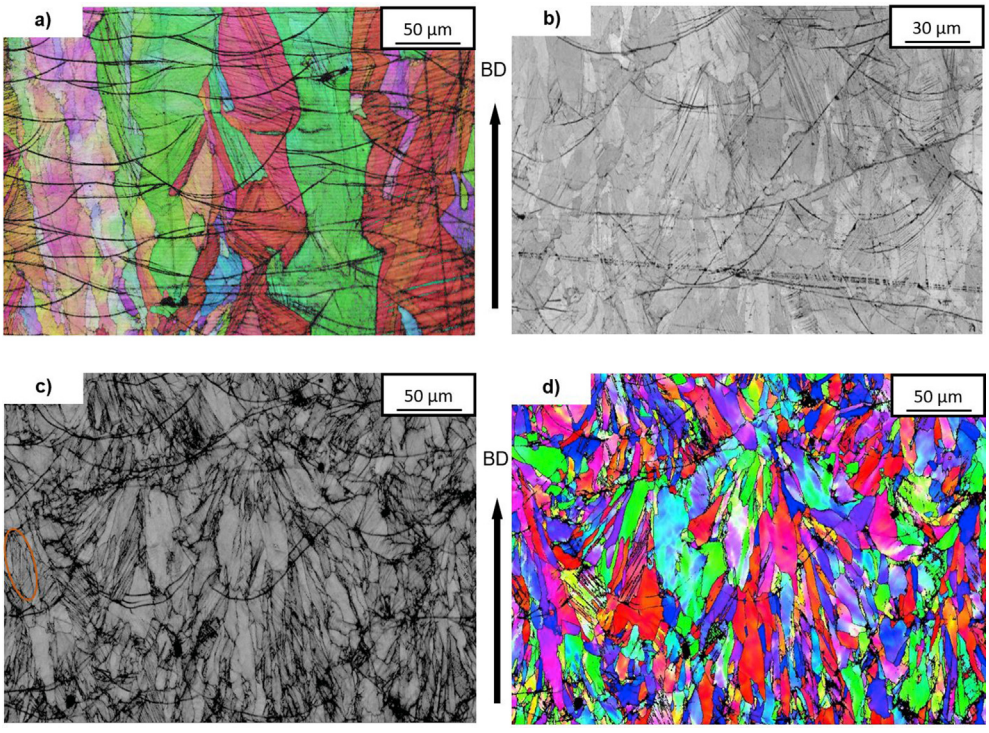

Fig. 6 – Overlapping band contrast and IPFZ maps on the 10% cold-rolled microstructure (A) a), band contrast maps of the microstructure (B) at 10% and 20% strain levels, respectively b) and c), IPF-Y map of the microstructure (B) at 20% strain level d). Building direction: Y_{EBSD}. Step size: 0.25–0.3 µm. Orange-circled zone shows the visible twins.

4. Discussion

4.1. As-built microstructure characteristics

At first, the two studied microstructures in this work present several differences in their as-built state. Microstructure (A) shows large size columnar grains, elongated along the building direction, and a strong texture ⟨110⟩ along the building direction. Microstructure (B) shows smaller size grains compared to microstructure (A), with a mean grain diameter of 20.3 μm compared to 102 μm for microstructure (A). The microstructure (B) is also crystallographically isotropic as previously observed [26].

These characteristics can be caused by several factors such as the chemical composition of the initial 316L powder used for the LPBF consolidation or the process parameters. Dryepondt et al. [26] mentioned the role of the LPBF parameters to change the as-built 316L microstructure properties from highly textured to almost isotropic. However, Chniouel [25] studied the as-built microstructure obtained from the powder used for (B) with the same machine and process parameters that were used in this work for (A). An isotropic, fine microstructure was obtained with equiaxed grains and no significant texture, as we obtained for sample (B) in the present study with other LPBF parameters. This would highlight the defining role of the powder on the final as-built microstructure properties, since the only changing parameter with sample (A) is the 316L powder that was used.

4.2. Grain morphology and size evolution upon cold-rolling until 20% sample thickness reduction

At first, no martensite was detected on all samples, either (A) or (B), which is in agreement with the results in literature. In fact, cold rolling with 20% reduction rate is not enough to initiate the martensitic transformation at room temperature (RT). Eskandari et al. [43] observed the same trend on standard wrought 316L cold rolled at 273 K. Strain-induced martensite was also seen on 30% cold-rolled 316L, as a volume fraction of 10% of strain-induced martensite phase was reported [42].

Pruncu et al. [32] reported a grain refinement on hot-forged LPBF 316L with a grain size reduced seven times for 30% plastic compressive strain at 1040 °C. Grain refinement, which is observed in standard wrought 316L [43], is also visible on AMed 316L microstructures. This grain refinement is especially observed in samples (A) with a reduction by half approximately of the mean grain diameter from 102 to 56 μm when cold-rolled at 20%. Nevertheless, some grains with a length higher than 300 μm still remain in the 20% cold-rolled microstructure. On the other hand, grain refinement is almost inexistent for the fine microstructure (B). Indeed, the mean grain size remains stable, ranging between 20.3 and 21.8 μm between the as-built and the cold-rolled states. This stability can be explained by the initial fine microstructure which cannot be refined further compared to sample (A). Therefore, an as-built fine microstructure has the advantage to be stable when cold-rolled concerning the grain refinement.

While mean grain diameter of samples (B) does not evolve significantly between the as-built and the cold-rolled states, the same trend is not observed concerning their morphology. Indeed, the mean aspect ratio increases to reach 0.34 when cold-rolled at 20% and the grains are re-oriented along the building direction. The mean grain orientation angle to X_{EBSD} increases from 63.5° to 78.6° between the as-built and the 20% cold-rolled microstructures. But, as mentioned above, no trend can be reliably drawn concerning the evolution of the grain morphology of samples (A) upon cold rolling, in regard to the evolution of both the mean aspect ratio and the mean grain orientation angle to X_{EBSD}. This can be explained by two consequences of cold-rolling causing in the end antagonist effects. One effect is actually the grain refinement seen before, which tends to generate smaller grains with a reduced aspect ratio. But, on the other hand, the rolling direction is collinear to the building direction, and consequently to the grains long-axis. This also tends to elongate pre-existing grains, and thus, to increase the grain aspect ratio. In the end, at least with this rolling direction orientation, the microstructure (A) keeps its grain morphology anisotropy after being cold-rolled at 20% and microstructure (B) becomes more anisotropic in terms of grain morphology when cold-rolled.

4.3. Texture and local misorientation evolution

The strong texture ⟨110⟩ along the building direction on sample (A) is reduced by cold rolling. Indeed, the peak intensity in the pole figures and the maximum of ODF figures are reduced by half between the as-built and the 10% cold-rolled samples (Fig. 4a and b). Hence, cold-rolling decreases the as-built texture intensity of microstructure (A). This trend is confirmed on the 20% cold-rolled sample as no additional texture is observed. Therefore, the strong ⟨110⟩ texture along the building direction still remains, at least until 20% thickness reduction. Concerning sample (B), the initial crystallographically isotropic as-built microstructure keeps its isotropy after 10% and 20% cold-rolling. Additionally, no significant texture evolution is observed after 20% thickness reduction. Thus, these both LPBF 316L steels show different behaviour regarding texture evolution upon cold rolling.

KAM maps show that cold rolling increases the local misorientation (Fig. 5) in both 316L steels. The KAM distribution for as-built samples have quite high angle values compared to those in the standard wrought 316L. Indeed, Beard et al. [45] reported an average KAM of 0.15° in the wrought 316L and of 0.60° in LPBF 316L steel. This KAM difference between wrought and LPBF 316L probably comes from the residual stresses which is a consequence of the LPBF process [46,47]. The KAM increase upon cold-rolling suggests that shear banding and dislocation multiplications could be predominant deformation modes in 316L LPBF steels.

These observations show that cold rolling induces local misorientations in as-AMed microstructure, which is common to conventional cold-rolled 316L [48].

4.4. Mechanical twinning in LPBF 316L steels

Another effect of cold rolling on both microstructures is the formation of mechanical twins, in addition to thermal twins inherited from the LPBF process. Mechanical twinning is activated at 10% deformation (Fig. 6a and b) but the activation

threshold is possibly at lower strains. Deformation twinning was observed on LPBF 316L steel under RT tensile loading [19,49]. This phenomenon is also observed in standard wrought 316L, starting from 5% straining degree [50]. From band contrast maps, cold rolling induces two effects: twinning of new grains and expansion of pre-existent mechanical twins as seen between 10% and 20% strain on microstructures (B) (Fig. 6b and c). At 20% strain, some grains exhibit two mechanical twinning variants (Fig. 6c), which is comparable to standard 316L [51]. More grains are twinned between 10% and 20% thickness reduction, as shown by the increasing twinned surface ratio. These phenomena are also observed on sample (A).

Considering that mechanical twinning promotes ductility [51], these AMed 316L steels are expected to show good ductility and long elongation capabilities [19,20,47]. An elongation to failure of approximately 50% was reported on different material grades [19,25]. Godec et al. [44] reported that the total elongation of the LPBF 316L material was 42% while it was 70% for the as-forged 316L. This high ductility and deformation capabilities are confirmed by the fact that both samples (A) and (B) can be cold-rolled to a maximum thickness reduction of 80% without any crack formation. Nevertheless, the EBSD study of such deformed samples did not allow us to draw any conclusions about the microstructure because of the very low indexation rate. However, on a thicker preform ($150 \times 60 \times 25$ mm^3) of sample (B), 50% is the maximum reachable strain because the piece bends so strongly that it cannot be cold-rolled further. This could probably come from the aforementioned residual stresses induced by the LPBF process that are not present in the traditional wrought 316L [46,47]. A stress relieving heat treatment could be a solution to relieve these stresses while keeping the LPBF specificities [15]. However, Ronneberg et al. [15] also mentioned that a heat treatment temperature superior to 900 °C during 1 h leads to the disappearance of the cellular sub-structure.

Hence, mechanical twinning is an important deformation mechanism in both 316L microstructures but shear banding and dislocation movements could be predominant.

4.5. *Regarding the molten pool boundaries (MPB)*

Another interesting observation concerns the role of molten pool boundaries (MPB). The grains can cross MPBs both in microstructures (A) and (B) (Figs. 3a and 6d) without showing any EBSD-measurable orientation change. This was also reported by Godec et al. [44] and Shifeng et al. [17]. The latter drew two types of MBPs: "layer–layer" MBPs where columnar grains keep the same orientation across, and "track–track" MBPs where a systematic orientation change was reported. Here, however, the "track–track" MPBs in our samples did not induce systematic orientation changes as explained by Shifeng et al. [17]. The local re-heating during the laser scan can explain the grain growth across the MPBs [15,25,44]. But grains can also stop at the MPBs as previously exposed [15]. In this work, this was especially observed in sample (B), leading to a lower mean grain size. The cold-rolled microstructures show that mechanical twins can also cross the MPBs (Fig. 6) if the grains cross them. Yet, even if the MPBs can be "transparent" to mechanical twinning, they form a chemical segregation zone with lower amount of Cr and Mo and a mechanical weakness in tensile deformations [15,44].

5. Summary and conclusions

In this study, the effects of cold rolling reduction at different rates on two different Laser Powder Bed Fusion (LPBF) microstructures are studied. Cold rolling process induces similar phenomena on both additively manufactured (AMed) 316L and standard wrought 316L, within the strain range of this study (maximum reduction rate of 20%): grain refinement, evolution of the initial texture and mechanical twinning along with an increase in the local misorientation, reflected by the increase of the Kernel Average Misorientation (KAM). This study shows that LPBF 316L has sufficient ductility to be cold-rolled, and more generally, cold-worked without any intermediate heat treatment after the LPBF production. More specifically, several conclusions can be drawn:

- ✓ The difference of initial microstructure regarding the mean grain size distribution and the texture intensity affects the extent of the grain refinement and the texture decay. As-built microstructure (B) shows initially smaller grains and nearly no texture compared to the as-built (A). Cold rolling does not change them for sample (B): the mean grain size remains stable until 20% thickness reduction and no preferential texture is detected. But the grain morphology becomes more anisotropic after cold-rolling along the building direction. However, the anisotropy in grain morphology and texture shown by the as-built microstructure (A) can be importantly hindered after 20% cold rolling.
- ✓ Mechanical twinning is induced by cold rolling in both studied AMed 316L steels, providing the ductility of the 316L LPBF parts. Its activity increases by increasing the cold rolling thickness reduction. However, shear banding and dislocation multiplication should be the predominant deformation mechanisms.
- ✓ The microstructural analysis reveals that many mechanical twins cross the molten pool boundaries. MPBs do not seem to act as obstacles to the formation and propagation of mechanical twins.

Further investigations on the mechanical properties of such cold-rolled preforms would be interesting since the 316L LPBF microstructure specific properties should remain: ductility along with high tensile strength. Furthermore, as the AMed parts show a strong microstructural anisotropy, especially sample (A), the effect of the rolling direction in regards to the building direction can be studied. The rolling test on a larger scale preform shows that the residual stresses in the as-built state can be problematic during high strain cold rolling, above 50%.

Declaration of Competing Interest

The authors declare that they have no known competing financial interests or personal relationships that could have appeared to influence the work reported in this paper.

Acknowledgements

The authors would like to thank all people who contributed directly or indirectly to this work: both laboratories LTMEx and LISL from CEA with specific thanks to J. Varlet and A. Chniouel.

REFERENCES

[1] Loto RT, Loto CA. Evaluation of the localized corrosion resistance of 316L austenitic and 430Ti ferritic stainless steel in aqueous chloride/sulphate media for application in petrochemical crude distillation units. Mater Res Express 2019;6:086516. https://doi.org/10.1088/2053-1591/ab1a11.

[2] Leng YX, Wang J, Yang P, Chen JY, Huang N. The adhesion and clinical application of titanium oxide film on a 316L vascular stent. Surf Coat Technol 2019;363:430–5. https://doi.org/10.1016/j.surfcoat.2018.12.021.

[3] Oliveira JP, Shen J, Zeng Z, Park JM, Choi YT, Schell N, et al. Dissimilar laser welding of a CoCrFeMnNi high entropy alloy to 316L stainless steel. Scr Mater 2022;206:114219. https://doi.org/10.1016/j.scriptamat.2021.114219.

[4] Shih CC, Shih CM, Su YY, Su L, Chang MS, Lin SJ. Effect of surface oxide properties on corrosion resistance of 316L stainless steel for biomedical applications. Corros Sci 2004;2:427–41. https://doi.org/10.1016/S0010-938X(03)00148-3.

[5] Sutow EJ. The influence of electropolishing on the corrosion resistance of 316L stainless steel. J Biomed Mater Res 1980;5:587–95. https://doi.org/10.1002/jbm.820140505.

[6] Was GS, Ukai S. Chapter 8 – austenitic stainless steels. In: Robert OG, Zinkle SJ, editors. Structural alloys for nuclear energy applications. Elsevier; 2019. p. 293–347. https://doi.org/10.1016/B978-0-12-397046-6.00008-3.

[7] Beck T, Blanc V, Escleine J-M, Haubensack D, Pelletier M, Phelip M, et al. Conceptual design of ASTRID fuel sub-assemblies. Nucl Eng Des 2017;315:51–60. https://doi.org/10.1016/j.nucengdes.2017.02.027.

[8] Bayoumi LS. Cold drawing of regular polygonal tubular sections from round tubes. Int J Mech Sci 2001;11:2541–53. https://doi.org/10.1016/S0020-7403(01)00056-X.

[9] Hirose T, Tanigawa H, Enoeda M, Akiba M. Effects of tube drawing on structural material for ITER test blanket module. Fusion Sci Technol 2017;4:839–43. https://doi.org/10.13182/FST07-A1596.

[10] Oliveira JP, LaLonde AD, Ma J. Processing parameters in laser powder bed fusion metal additive manufacturing. Mater Des 2020;193:108762. https://doi.org/10.1016/j.matdes.2020.108762.

[11] Sames WJ, List FA, Pannala S, Denhoff RR, Babu SS. The metallurgy and processing science of metal additive manufacturing. Int Mater Rev 2016;5:315–60. https://doi.org/10.1080/09506608.2015.1116649.

[12] Kumar LJ, Nair CG. Current trends of additive manufacturing in the aerospace industry. In: Wimpenny DI, Pandey PM, Kumar LJ, editors. Advances in 3D printing & additive manufacturing technologies. Singapore: Springer; 2017. p. 39–54. https://doi.org/10.1007/978-981-10-0812-2_4.

[13] Gu DD, Meiners W, Wissenbach K, Poprawe R. Laser additive manufacturing of metallic components: materials, processes and mechanisms. Int Mater Rev 2012;3:133–64. https://doi.org/10.1179/1743280411Y.0000000014.

[14] DebRoy T, Mukherjee T, Milewski JO, Elmer JW, Ribic B, Blecher JJ, et al. Scientific, technological and economic issues in metal printing and their solutions. Nat Mater 2019;18:1026–32. https://doi.org/10.1038/s41563-019-0408-2.

[15] Ronneberg T, Davies CM, Hooper PA. Revealing relationships between porosity, microstructure and mechanical properties of laser powder bed fusion 316L stainless steel through heat treatment. Mater Des 2020;189:108481. https://doi.org/10.1016/j.matdes.2020.108481.

[16] Kurzynowski T, Gruber K, Stopyra W, Kuznicka B, Chlebus E. Correlation between process parameters, microstructure and properties of 316L stainless steel processed by selective laser melting. Mater Sci Eng A 2018;718:64–73. https://doi.org/10.1016/j.msea.2018.01.103.

[17] Shifeng W, Shuai L, Qingsong W, Yan C, Sheng Z, Yusheng S. Effect of molten pool boundaries on the mechanical properties of selective laser melting parts. J Mater Process Technol 2014;11:2660–7. https://doi.org/10.1016/j.jmatprotec.2014.06.002.

[18] Liverani E, Toschi S, Ceschini L, Fortunato A. Effect of selective laser melting (SLM) process parameters on microstructure and mechanical properties of 316L austenitic stainless steel. J Mater Process Technol 2017;249:255–63. https://doi.org/10.1016/j.jmatprotec.2017.05.042.

[19] Pham MS, Dovgyy B, Hooper PA. Twinning induce plasticity in austenitic stainless steel 316L made by additive manufacturing. Mater Sci Eng A 2017;704:102–11. https://doi.org/10.1016/j.msea.2017.07.082.

[20] Natali S, Brotzu A, Pilone D. Comparison between mechanical properties and structures of a rolled and a 3D-printed stainless steel. Materials 2019;23:3867. https://doi.org/10.3390/ma12233867.

[21] Wang YM, Voisin T, McKeown JT, Ye J, Calta NP, Li Z, et al. Additively manufactured hierarchical stainless steels with high strength and ductility. Nat Mater 2018;17:63–71. https://doi.org/10.1038/nmat5021.

[22] Donadille C, Valle R, Dervin P, Penelle R. Development of texture and microstructure during cold-rolling and annealing of F.C.C alloys: example of an austenitic stainless steel. Acta Metall 1989;6:1547–71. https://doi.org/10.1016/0001-6160(89)90123-5.

[23] Sun SH, Ishimoto T, Hagihara K, Tsutumu Y, Hanawa T, Nakano T. Excellent mechanical and corrosion properties of austenitic stainless steel with a unique crystallographic lamellar microstructure via selective laser melting. Scr Mater 2019;159:89–93. https://doi.org/10.1016/j.scriptamat.2018.09.017.

[24] Sun Z, Tan P, Tor SB, Chua CK. Simultaneously enhanced strength and ductility for 3D-printed stainless steel 316L by selective laser melting. NPG Asia Mater 2018;10:129–36. https://doi.org/10.1038/s41427-018-0018-5.

[25] Chniouel A. Étude de l'élaboration de l'acier inoxydable 316L par fusion laser sélective sur lit de poudre : influence des paramètres du procédé, des caractéristiques de la poudre, et de traitements thermiques sur la microstructure et les propriétés mécaniques. Thèse de doctorat de l'Université Paris-Saclay. 2019 [TEL: tel-02421550].

[26] Dryepondt S, Nandwana P, Fernandez-Zelaia P, List F. Microstructure and high temperature tensile properties of 316L fabricated by laser powder-bed fusion. Addit Manuf 2021;37:101723. https://doi.org/10.1016/j.addma.2020.101723.

[27] Byun TS, Garrison BE, McAlister MR, Chen X, Gussev MN, Lach TG, et al. Mechanical behaviour of additively manufactured and wrought 316L stainless steel before and after neutron irradiation. J Nucl Mater 2021;548:152849. https://doi.org/10.1016/j.jnucmat.2021.152849.

[28] Shen J, Zeng Z, Nematollahi M, Schell N, Maawad E, Vasin RN, et al. In-situ synchrotron X-ray diffraction analysis of the elastic behaviour of martensite and H-phase in a

NiTiHf high temperature shape memory alloy fabricated by laser powder bed fusion. Addit Manuf Lett 2021;1:100003. https://doi.org/10.1016/j.addlet.2021.100003.
[29] Cherry JA, Davies HM, Mehmood S, Lavery NP, Brown SGR, Sienz J. Investigation into the effect of process parameters on microstructural and physical properties of 316L stainless steel parts by selective laser melting. Int J Adv Manuf Technol 2015;76:869–79. https://doi.org/10.1007/s00170-014-6297-2.
[30] Frazier WE. Metal additive manufacturing: a review. J Mater Eng Perform 2014;23:1917–28. https://doi.org/10.1007/s11665-014-0958-z.
[31] Jiang J, Hooper P, Li N, Luan Q, Hopper C, Ganapathy M, et al. An integrated method for net-shape manufacturing components combining 3D additive manufacturing and compressive forming processes. Procedia Eng 2017;207:1182–7. https://doi.org/10.1016/j.proeng.2017.10.1050.
[32] Pruncu CI, Hopper C, Hooper PA, Tan Z, Zhu H, Lin J, et al. Study of the effects of hot forging on the additively manufactured stainless steel preforms. J Manuf Process 2020;57:668–76. https://doi.org/10.1016/j.jmapro.2020.07.028.
[33] Sizova I, Bambach M. Hot workability and microstructure evolution of pre-forms for forgings produced by additive manufacturing. Procedia Eng 2017;207:1170–5. https://doi.org/10.1016/j.proeng.2017.10.1048.
[34] Bambach M, Sizova I, Emdadi A. Development of a processing route for Ti-6Al-4V forgings based on preforms made by selective laser melting. J Manuf Process 2019;37:150–8. https://doi.org/10.1016/j.jmapro.2018.11.011.
[35] Bambach M, Sizova I, Szyndler J, Bennett J, Hyatt G, Ciao J, et al. On the hot deformation behaviour of Ti-6Al-4V made by additive manufacturing. J Mater Process Technol 2021;228:116840. https://doi.org/10.1016/j.jmatprotec.2020.116840.
[36] Bambach M, Sizova I, Silze F, Schnick M. Hot workability and microstructure evolution of the nickel-based superalloy Inconel 718 produced by laser metal deposition. J Alloy Compd 2018;740:278–87. https://doi.org/10.1016/j.jallcom.2018.01.029.
[37] Colegrove PA, Coules HE, Fairman J, Martina F, Kashoob T, Mamash H, et al. Microstructure and residual stress improvement in wire and arc additively manufactured parts through high-pressure rolling. J Mater Process Technol 2013;10:1782–91. https://doi.org/10.1016/j.jmatprotec.2013.04.012.
[38] Martina F, Colegrove PA, Willams SW, Meyer J. Microstructure of interpass rolled wire + arc additive manufacturing Ti-6Al-4V components. Metall Mater Trans A 2015;46:6103–18. https://doi.org/10.1007/s11661-015-3172-1.
[39] Martina F, Roy MJ, Szost BA, Terzi S, Colgrove PA, Willams SW. Residual stress of as-deposited and rolled wire+arc additive manufacturing Ti-6Al-4V components. Mater Sci Technol 2016;14:1439–48. https://doi.org/10.1080/02670836.2016.1142704.
[40] Wang X, Muniz-Lerma JA, Sanchez-Mata O, Shandiz MA, Brochu M. Microstructure and mechanical properties of stainless steel 316L vertical struts manufactured by laser powder bed fusion process. Mater Sci Eng A 2018;736:27–40. https://doi.org/10.1016/j.msea.2018.08.069.
[41] Liu J, Song Y, Chen C, Wang X, Li H, Zhou C, et al. Effect of scanning strategies on the microstructure and mechanical behaviour of 316L stainless steel fabricated by selective laser melting. Mater Des 2020;186:108335. https://doi.org/10.1016/j.matdes.2019.108355.
[42] Mao Q, Gao B, Li J, Huang Z, Li Y. Enhanced tensile properties of 316L steel via grain refinement and low-strain rolling. Mater Sci Technol 2019;12:1497–503. https://doi.org/10.1080/02670836.2019.1630088.
[43] Eskandari M, Najafizadeh A, Kermanpur A. Effect of strain-induced martensite on the formation of nanocrystalline 316L stainless steel after cold rolling and annealing. Mater Sci Eng A 2009;1–2:46–50. https://doi.org/10.1016/j.msea.2009.04.038.
[44] Godec M, Zaefferer S, Podgornik B, Sinko M, Tchernychova E. Quantitative multiscale correlative microstructure analysis of additive manufacturing of stainless steel 316L processed by selective laser melting. Mater Charact 2020;160:110074. https://doi.org/10.1016/j.matchar.2019.110074.
[45] Beard W, Lancaster R, Adams J, Buller D. Fatigue performance of additively manufactured stainless steel 316L for nuclear applications. Austin, United States. In: Bourell DL, Beaman JJ, Crawford RH, Fish S, Kovar D, Seepersad CC, editors. Proceedings of the 30th annual international solid freeform fabrication symposium; 2019. p. 2144–55 [ResearchGate: Fatigue_Performance_of_Additively_Manufactured].
[46] Liu Y, Yang Y, Wang D. A study on the residual stress during selective laser melting (SLM) of metallic powder. Int J Adv Manuf Technol 2016;87:647–56. https://doi.org/10.1007/s00170-016-8466-y.
[47] Shamsujjoha M, Agnew SR, Fitz-Gerald JM, Moore WR, Newman TA. High strength and ductility of additively manufactured 316L stainless steel explained. Metall Mater Trans A 2018;49:3011–27. https://doi.org/10.1007/s11661-018-4607-2.
[48] Chen J, Xiao Q, Lu Z, Ru X, Han G, Tian Y, et al. The effects of prior-deformation on anodic dissolution kinetics and pitting behavior of 316L stainless steel. Int J Electrochem Sci 2016;11:1395–415 [ResearchGate: The_Effects_of_Prior-Deformation].
[49] Woo W, Jeong JS, Kim DK, Lee CM, Choi SH, Suh JY, et al. stacking fault energy analyses of additively manufactured stainless steel 316L and CrCoNi medium entropy alloy using in situ neutron diffraction. Sci Rep 2020;10:1350. https://doi.org/10.1038/s41598-020-58273-3.
[50] Müllner P, Solenthaler C, Uggowitzer P, Speidel MO. On the effect of nitrogen on the dissolution structure of austenitic stainless steel. Mater Sci Eng A 1993;1–2:164–9. https://doi.org/10.1016/0921-5093(93)90655-X.
[51] Xue Q, Cerreta EK, Gray GT. Microstructural characteristics of post-shear localization in cold-rolled 316L stainless steel. Acta Mater 2007;2:691–704. https://doi.org/10.1016/j.actamat.2006.09.001.